Saturation Point Structure of Marine Stratocumulus Clouds

REINOUT BOERS*

Laboratory for Atmospheres, NASA/Goddard Space Flight Center, Greenbelt, Maryland

ALAN K. BETTS

West Pawlet, Vermont

ABSTRACT

The microstructure of a Pacific stratocumulus capped boundary layer was examined. The boundary layer flow was over an area of sea-surface temperature gradient, so that no steady state was present. Conserved variable diagrams showed a complex structure with one branch of the mixing line extending from the mixed layer saturation point to the ocean surface saturation point, a second branch in the cloud layer and a third upward into the inversion. They correspond well with a conceptual model for the unstable, radiatively cooled cloud topped boundary layer. Saturation point pairs for ascending and descending branches of the internal boundary layer circulation were isolated by a simple conditional sampling technique. Pair separation decreased downward towards the surface, as did the variance around the mean ascent and descent values. Also, the variance was smaller for the ascending branch than for the descending branch. Spectral analysis of the saturation pressure showed that the primary circulation scale was 5 km, the same scale that was observed by lidar observations of cloud tops. A budget diagram for the time-dependent boundary layer is used to derive the time evolution of the layer and the entrainment rate using radiative flux estimates from a model incorporating cloud top heights from the lidar, and cloud liquid water and temperature from a mixing line model. A reasonable cloud top entrainment rate of 1 cm s^{-1} was obtained. The internal convective circulation velocity was found to be an order of magnitude higher corresponding to an internal circulation time scale of about 1 hour. The external adjustment time of the layer was 10 hours and the lag of the layer mean from equilibrium agreed with the advection over a 3°C warmer sea surface in 10 hours.

1. Introduction

In a series of papers, (Betts, 1982a,b, 1983, 1985a, 1986) a conserved variable method was developed to study processes of vertical mixing. Air parcels are characterized by their saturation point (SP) properties, such as saturation pressure, potential temperature, and equivalent potential temperature, which are conserved under dry or moist adiabatic motion, and, conserved extensively in mixing processes. For example, if the cloud-topped boundary layer (CBL) has distinct source regions of constant SP such as the ocean surface or the dry inversion air above its top, the state of the atmosphere in between can be conveniently expressed in terms of linear variations along a mixing line of the conserved SP properties. Deviations from this mixing line are then caused by radiation, precipitation, and/ or lack of stationarity. Conserved variable methods

have been used in many conceptual models of the cloudy boundary layer (Stage and Businger, 1981; Randall, 1980a; Schubert et al., 1979; Lilly, 1968; Albrecht et al., 1979). Betts (1986) has suggested that clear, partly cloudy, and cloudy boundary layers, including the trade wind boundary layer can be described in a unified way using gradients of SP parameters.

The experimental study of stratocumulus layers is of great interest for the validation of proposed parameterizations of cloud layers in global circulation models (Suarez et al., 1983). Several studies have examined the microstructure of these clouds in great detail (Nicholls and Leighton, 1986; Nicholls and Turton, 1986; Slingo et al., 1982). However, few observational studies exist that confirm the value of the SP analysis for boundary layer clouds (Hanson, 1984; Betts, 1985b, 1986; Betts and Simpson, 1987; Betts and Albrecht, 1987). The purpose of this paper is to study the SP structure of the same stratocumulus layer as the one for which high altitude lidar observations were presented by Boers et al. (1988, abbreviated as BSH). In BSH it was found that the top of the cloud deck presently under study sloped gradually upward in an east-west, north-south direction from 750 m in the northwest to 1000 m in the southeast. Clouds also thickened

---

* Also affiliated: Department of Meteorology, University of Maryland.

Corresponding author address: Dr. Reinout Boers, NASA/Goddard Space Flight Center, Code 617, Greenbelt, MD 20771.

in the same direction since the variation in cloud base was much less. Local cloud top variations were of the order of 80 m. Spectral analysis of the lidar observations revealed dominant horizontal structures of the order of 4.5–5.0 km in diameter, which agreed very well with observations of visible radiance independently measured by the Multispectral Cloud Radiometer, co-aligned and synchronized with the lidar.

2. Experimental design and data processing

a. Data collection

The experiment was conducted over the Pacific Ocean near San Francisco, and it involved NASA's ER-2 aircraft and the Wyoming King Air (see BSH for a detailed account of the experimental plan and flight design). Data was taken on 28 September 1983 between 1200 and 1600 PST at 124°W, 36.6°N. For the SP analysis, we used the 1 Hz in situ data gathered aboard the King Air. Temperature was measured by the reverse flow thermometer which is minimally affected by probe wetting. Three instruments were on-board to measure liquid water content: the FSSP, Johnson-Williams probe, and the CSIRO-liquid water meter. The FSSP suffered from irregular offset problems, while the CSIRO-probe recordings had random sections of missing data. Therefore, only the Johnson-Williams probe was used to determine liquid water content. Crucial to the SP analysis was the determination of the dewpoint. Since the fast response Lyman-Alpha nephelometer did not work properly, all dewpoint information was derived from the Cambridge dewpoint unit. A nose-boom gust probe recorded horizontal and vertical wind speed and direction. Vertical wind speed variations were not used in our analysis.

b. Dewpoint correction procedure

Because of the well-known response problems of the Cambridge dewpoint unit (model 137-C3) (Cooper, 1978) great care had to be taken in the preprocessing of the data to assure that correct dewpoint values were obtained for the SP analysis. The method to measure dewpoint is to optically detect the intensity of light reflected off condensate that coats a small mirror surface. A servosystem, coupled to the optical detector, electrically controls the temperature of the mirror, so that a constant thickness of the coating is maintained on the mirror. The temperature of the mirror is independently measured, and yields the actual dewpoint values. Manufacturers' specifications give a slow response rate of 3°C s^{-1}. However, other known characteristics include variable response and stability problems depending on the thickness of the coating and offset variations (Duchon and Goers, 1976). Initial examination of the dewpoint data revealed that all of these problems were, in fact, present. The data tape supplied 1-second dewpoint data.

The in-cloud dewpoint values at saturation were offset from the actual temperature by about 0.6°C. This offset is most likely caused by the instrument response function. Unfortunately, there is no analytical way to remove the response function from the data since its exact functional form is unknown. Our procedure to remove the instrument offset was to determine the average measured dewpoint and in-cloud temperature for the in-cloud data with liquid water content above 0.02 g m^{-3}. This assures that the air is saturated and dewpoint and temperature should be approximately the same. The difference between the two values was added to the dewpoint. Offset values showed small variations from flight leg to flight leg. Figure 1 (upper panel) shows the temperature and dewpoint with only this offset removed. Some sections of the data contained rapid dewpoint oscillations of 0.2–0.3°C at 0.33 Hz. This problem has been attributed to the condensate coating being too thin (Cooper, 1978). This oscillation could be conveniently removed by applying a three-point smoother on the data (second panel in Fig. 1). Our ad hoc scheme to account for the slow response time of the instrument was to shift the time axis of the dewpoint data 2 seconds, that is, $T_{dew}(t + 2) = T_{dew}(t)$. This seemingly simplistic approach, which is justified in appendix A gave very good results in the SP analysis. Friehe and Grossman (1986) suggested the same procedure after comparing a similar instrument with a fast response Lyman Alpha hygrometer. The second panel of Fig.
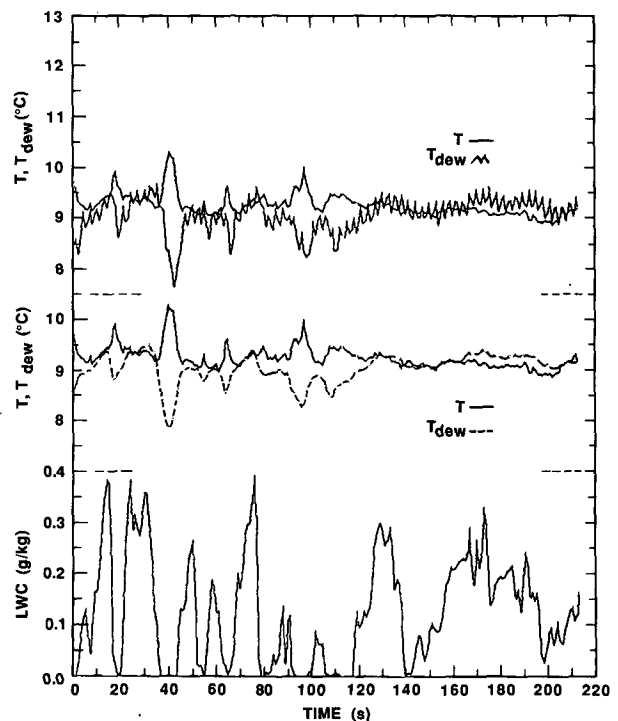

FIG. 1. Temperature, dewpoint and liquid water
as a function of time.

1 shows the corrected dewpoint, and temperature, and the lowest panel the liquid water trace for a horizontal flight leg through the upper portion of the cloud layer. At a number of points, the airplane briefly enters the inversion, for example, at $t = 40$ s, $t = 95$ s, and $t = 115$ s. At those times, the temperature increased with a corresponding decrease in dewpoint. It is clear that some of the response problems have been corrected by our procedure as the minima in dewpoint very closely follow the maxima in temperature. However, dewpoints remain well below the actual temperature for cloudy patches between $t = 80$ s and $t = 110$ s. Although this seems to be caused by a failure of our procedure, it might very well be that these measurements are representative of unsaturated air parcels which contain some liquid water. Such transitory parcels could be encountered near the inversion where dry air is engulfed into the cloudy convective boundary layer (CBL). As we shall see below, a special procedure is needed to determine saturation points for such parcels. There are also sections in the data where the dewpoint is actually higher than the temperature, for example, between $t = 160$ s and $t = 200$ s. For these periods, we used temperature instead of dewpoint to compute SP values.

c. Derived parameters: saturation point and conserved variables

We derived saturation pressure (p^*) and temperature (T^*) from the dewpoint and temperature data. The saturation pressure of an air parcel (Betts, 1982a) is defined as that atmospheric level where the parcel just reaches saturation by adiabatic ascent or descent and the saturation temperature is the parcel temperature at that level. Thus, these parameters are conserved under adiabatic translation of the air parcel. The SP notation is unusually concise. For example, an adiabatic mixed layer of several hundred meters thickness, which is typically represented by a vertical profile of temperature and humidity, reduces to a single point in SP coordinates (Betts, 1982a, Hanson, 1984). For unsaturated parcels, the SP is the intersection of the dry adiabat through the parcel temperature and the constant q line through the dewpoint. For cloudy saturated parcels, it is the intersection of the moist adiabat through the parcel temperature with the q isopleth equal to the total water mixing ratio (vapor + liquid). This represents a parcel sinking along a moist adiabat until all its liquid water has just evaporated (Betts, 1982a).

For unsaturated parcels containing some liquid water, we use the procedure shown in Fig. 2. Dewpoint and temperature were used to determine the lifting condensation level. Next, the liquid water content (LWC) was used to lower the parcel along a moist adiabat to give the final saturation point shown. This procedure essentially combines both procedures for wet
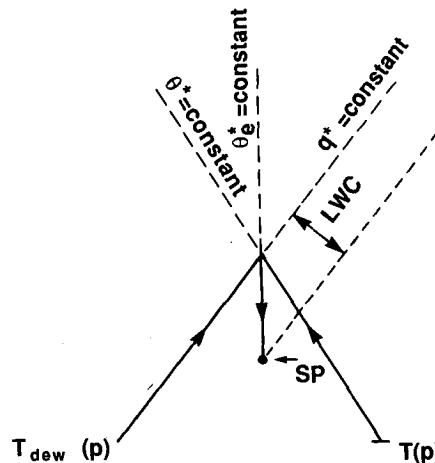

FIG. 2. Determination of SP for unsaturated parcels containing liquid water, p_1 is the pressure of the air parcel.

and dry air parcels, and is equivalent to evaporating the liquid water into the unsaturated air to give a thermodynamic equilibrium point. Finally, we computed θ^*, θ_e^* and q^*, the conserved variables at the saturation point. For unsaturated air θ^* is just the potential temperature θ, while it becomes θ_l, the liquid water potential temperature for cloudy air. The q^* is the total water and θ_e^*, the equivalent potential temperature.

Because of the small liquid water content found for this case study, the largest contribution to errors in SP variables is caused by uncertainties in dewpoint measurements. These errors are caused by uncertainties in the offset values and by the variable amplitude response due to the instrument and the three point filter. Although we outlined (in §2b) a procedure to correct the dewpoint it is likely that some residual error in the point-by-point determination of SP variables remain. There is much larger variability caused by the inhomogeneities in the CBL. By averaging, we will show that a consistent CBL budget analysis can be performed.

d. Conceptual model

Three main concepts will be used to analyze the mean gradients within the CBL, the internal circulation and to construct budget diagrams for the time-dependence of the layer.

1) MEAN GRADIENTS WITH p

It is convenient to analyze the departure from a well-mixed structure (which would have an SP independent of pressure) in terms of the variation of saturation level, p^*, with pressure, p, (Betts, 1982b, 1985a).

A particularly convenient parameter derived from our analysis is $\beta = dp^*/dp$. Its value lies in that it relates changes of conserved parameters in p and p^* coordinates. Since air near the surface is unsaturated, the existence of a cloud layer requires $0.0 < \beta < 1.0$. Here

$\beta = 0$ represents a well-mixed layer and a larger value indicates a less well mixed structure. Betts (1986) has suggested that the convective boundary layer structure can be parameterized in global models in terms of a mixing line and a specified vertical profile of β. It was therefore of interest to us to determine mean values of β for the cloud and subcloud layers.

2) CIRCULATION MODEL

Of great interest is the internal circulation characteristics of the cloud and subcloud layers. While different air parcels at the same atmospheric level generally have fluctuating SP values because of the natural variability of the atmosphere, it is instructive to separate SP values into updraft and downdraft values by performing an analysis based on the conditional sampling of variables (Greenhut and Khalsa, 1982). Such analysis can be accomplished by separating SPs based on the sign of their vertical velocity. The separation between SP values (Betts, 1983) can be understood in terms of the circulation speed of the ascending and descending portions of the large eddies. For a given convective flux, if the separation is large, the circulation is slow; and conversely if the separation is small, the circulation is fast. The distribution of SP values around their mean tells about the homogeneity of the updraft and downdrafts. In practice, the conditional analysis was performed by separating SPs according to the magnitude of their horizontal wind velocity. As explained in section 3d, this turned out to be a much better indicator of updraft and downdraft parcels than vertical velocity, since the wind shear between the CBL and the atmosphere aloft was large. Betts (1985a) suggested that shifts of the SP means with height, and the variation of SP about the mean are related to mixing between branches. Therefore, we examine the distribution of SP as a function of height.

3) BUDGET DIAGRAMS

Betts (1983) showed how budget diagrams could be constructed for time-dependent mixed layers to show the surface, entrainment, and radiative fluxes and the lag of the mixed layer SP from equilibrium. Figure 7 of that paper also showed how the SPs associated with the ascending and descending branches of the internal circulation were related to the time-dependence of the layer. We shall use and extend these concepts here to a partially mixed layer, and extract the entrainment rate, internal circulation velocity, and time-dependence of the layer from the aircraft data and a radiation model (see section 4 and appendix B).

3. Analysis of CBL structure

a. Overview

Boers et al. (1988) discussed the aircraft pattern and morphology of the cloud field. The experiment was

conducted in a northerly flow in a region of considerable north–south sea surface temperature gradient (3°C in 400 km), so we have reason to believe the CBL was not in a steady state. The lidar data (BSH) shows periodic structures in the cloud field and a variation in the height of cloud-tops across the aircraft pattern. Our primary objective, to extract mean profiles and characteristics for the CBL thermodynamic structure is not therefore straightforward, and several averaging procedures were attempted. The aircraft data falls into two types: long quasi-horizontal flights around a box pattern, primarily within the cloud layer itself near 925 hPa (1 hPa = 1 mb); and ascent or descent soundings from near the surface to above the cloud top. The horizontal legs were used to explore the spectral structure of the thermodynamic variations. Both soundings and horizontal legs were merged to generate mean profiles and to study the spread of SP about the mean for ascending and descending air at different pressure levels. We shall first present some individual profiles to acquaint the reader with the data and SP mapping.

b. Two examples

Figure 3a shows a temperature, dewpoint, and liquid water content time series from an aircraft ascent through the CBL and the inversion. The data was taken in the northeastern corner of the experimental area. The record between 80 and 165 s corresponds to broken cloud cover between heights of 600 to 800 m (940–920 hPa). At 800 m (165 s), the aircraft entered the inversion. Temperature increases while the dewpoint decreases. However, another moist layer is encountered just above the inversion where the specific humidity increases. The associated SP points are plotted on Fig. 3b on a θ^*-q^* plot. Saturation points from data below the inversion have $p^* > 910$ hPa. There appears to be a kink in the SP cluster at $p^* = 940$ hPa. Data with $p^* > 940$ hPa forms a cluster almost parallel to the line of constant potential temperature, while for $p^* < 940$ hPa, the SPs extend upwards smoothly into the inversion mixing line which is more parallel to the wet adiabat. The moist layer above the inversion is very much amplified in this diagram as the sudden kink at the top of the figure. Betts and Albrecht (1987) found similar SP reversals for FGGE data. Figure 3c shows a plot of saturation point pressure p^* versus pressure p. It is seen that for pressures between 925 and 985 hPa, p^* increases from 935 to 960 hPa. On the average $\beta = dp^*/dp = 0.4$, indicating that the CBL is not well mixed. Data points represented by circles on these plots are associated with parcels with liquid water < 0.02 g m^{-3}. Those represented by plusses are associated with parcels with liquid water ≥ 0.02 g m^{-3}.

Figures 4a, b, c show similar data, from an ascent for the northwestern corner of the area. Figure 4a shows that the cloud penetrated by the aircraft is solid, with an initial increase of the liquid water content closely
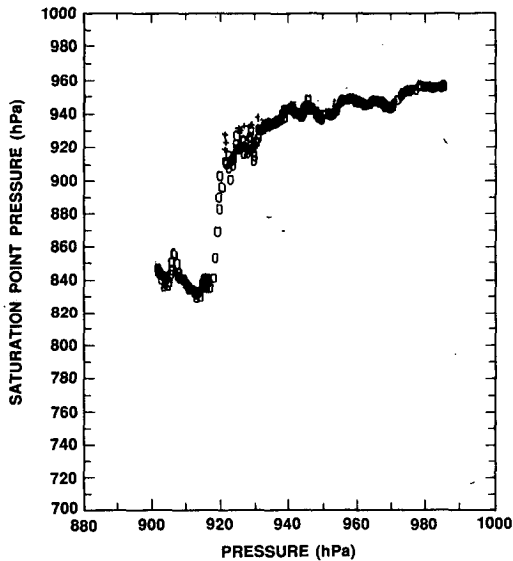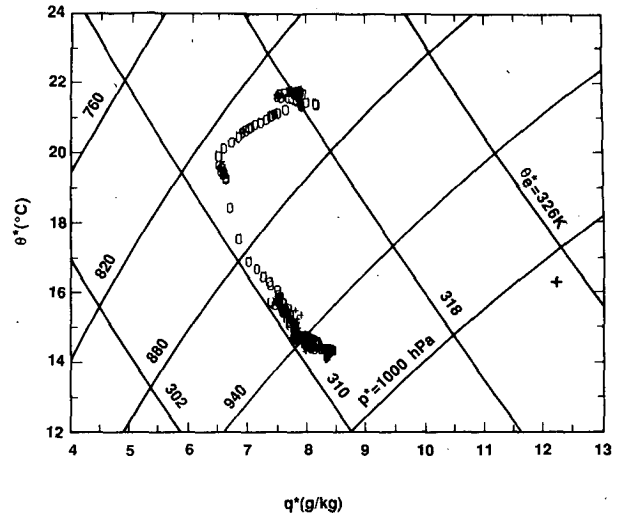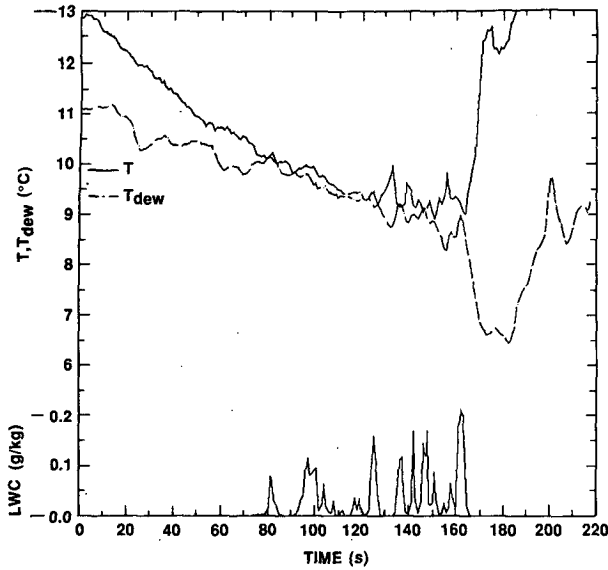
FIG. 3. (a) Temperature, (T) dewpoint (T_{dew}) liquid water from ascent leg in northeast corner of experimental area. T is indicated by solid line, T_{dew} by broken line. (b) Skew-T diagram of SPs corresponding to data shown in (a). (c) p^* versus p plot for data corresponding to (a).

approaching the adiabatic law. Near the inversion, however, liquid water values go down, well before the actual inversion has been reached. This indicated intense mixing of the cloud top with the inversion air. Cloud base was at 560 m (945 hPa) while cloud top was at 880 m (911 hPa). Thus, cloud thickness was well over 300 m in this region. These observations are consistent with the lidar observations presented by BSH which indicated higher cloud top heights toward the west with decreased transparency. Figure 4b shows a similar cluster of SPs as shown in Fig. 3b. All points representing CBL air are densely packed at the bottom of the plot. Since the layer was drier in this region, this point cluster has been displaced in comparison to Fig. 3b, nearly along a line of constant potential temperature. Figure 4c shows that p^* is almost constant with pressure for the CBL air. Near the cloud top, it grad-

ually drops off with decreasing pressure with the most dramatic drop as the aircraft penetrates the inversion. Clearly, this figure represents a well developed solid cloud layer with a nearly well-mixed structure. These results are consistent with the photographic evidence and the lidar signals presented by BSH.

c. Vertical profiles

Panel (a) of Fig. 5 shows a scatter plot of the SPs of all the aircraft data. There is a considerable spread of the data associated with variations in sea surface temperature (there is a northerly low level flow across a north–south temperature gradient), variations in cloud-base and cloud top height and inhomogeneities in the atmosphere above the inversion.

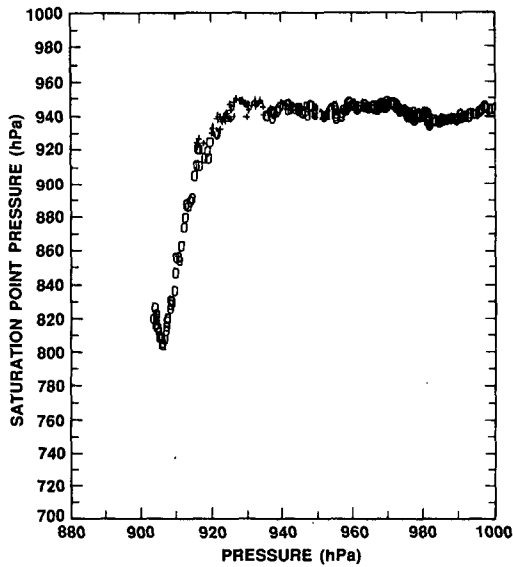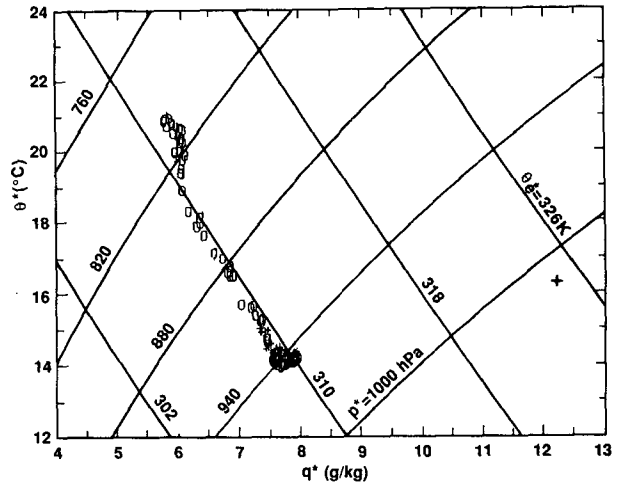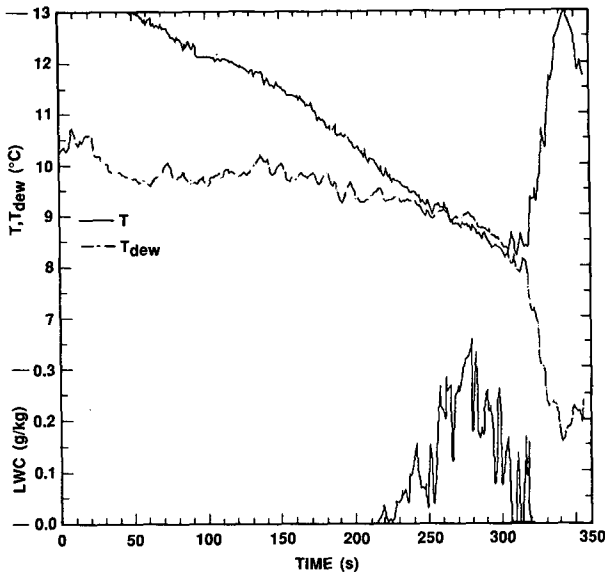Our primary objective was to extract some mean

FIG. 4. As in Fig. 3a, b, c but for the ascent in northwest corner of experimental area.

CBL characteristics. The data were first averaged to obtain mean thermodynamic profiles for the CBL. Several averaging methods were attempted with interesting results. We computed saturation temperature and pressure for each data value (every second) and grouped the data in three different ways. Figure 5b shows the data from Fig. 5a averaged in 5 hPa pressure bins, Figure 5c averaged in 5 hPa bins in p^*, and Fig. 5d averaged in 0.5°C bins in θ^*. Selected mean SPs are labeled with the corresponding mean pressure level. Superficially they show some similarities, but they are different because of the different groupings of the data. We shall discuss each average in turn, and then produce a composite mean profile through the CBL.

1) THE p AVERAGE

The simple p average (in intervals of 5 hPa) (Fig. 5b) represents the vertical structure well through most of the layer. It smooths through horizontal variations of T and q in the subcloud layer. It shows a dense clustering of points representing air in the subcloud layer, and a gradient through the cloud and inversion layers. Some points are labeled with their average pressure. The subcloud layer gradient is not readily visible in Fig. 5b because of the clustering of points near $q = 8$ g kg^{-1}. Figure 8 (see later) on an expanded scale (and with more averaging) will show the gradients through the CBL more clearly.
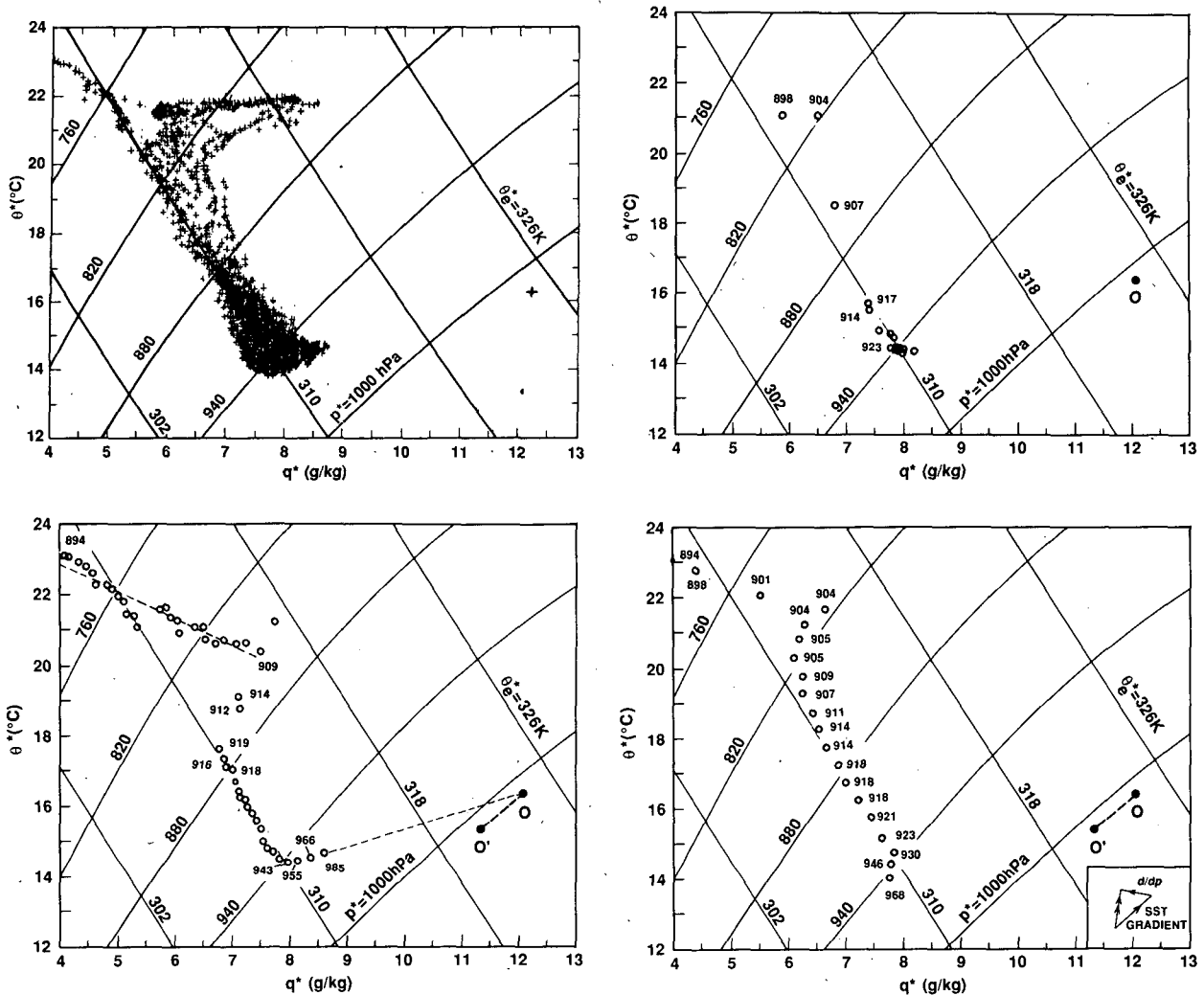
FIG. 5. (a) Scatter plot of SPs of all data. (b) Data from (a) averaged (b) in p-bins of 5 hPa,
(c) in p^*-bins of 5 hPa and (d) in θ^*-bins of 0.5°C.

2) THE p^* AVERAGE

This average (Fig. 5c) shows two major differences from the p average in the subcloud layer and above the inversion where the SPs are spread out along a line. A dashed extension of the distribution in the subcloud layer points approximately to the SP (marked O) of the ocean surface temperature (SST). We interpret this as follows: the subcloud data has been sorted by p^* and the parcels with the highest p^* (closest to the surface pressure) will be air that has ascended in thermals from near the surface and will be closest to surface layer properties, O, so that the distribution of SPs represent different mixtures of surface air, and hence lie along a mixing line (Betts, 1983). The flight pattern lies across a strong north–south SST gradient. The O corresponds to (17°C, 1008 hPa) the SST below the pattern, and O' to (16°C, 1008 hPa), the SST approximately 100

km to the north. The layer is unlikely to be in a steady state since this corresponds to an advection time of only 2.3 hours.

This p^* average does not represent a mean vertical gradient for the subcloud layer. There is a gradient of p with SP (see small numbers on Fig. 5c), but this reflects simply that the highest p^* values are statistically closer to the surface. For example, the extreme point (with a mean pressure of 985 hPa) is the average SP of parcels which had $955 < p^* < 960$ hPa, while other air parcels near this pressure with $p^* < 955$ hPa are excluded from this average.

Above the inversion, there is a broad scatter of the data along a band, much more pronounced than in Fig. 5b. It represents again the sorting by p^* of the inhomogeneities in the air above the inversion, this time in quite a narrow range of pressure (894–909 hPa). We see there are large variations in q^* from 4 to 7 g

kg^{-1} above the inversion ($\theta^* > 20°C$), and the varia-
tions of θ^*, q^* are approximately along a mixing line
(shown dashed). Betts (1984) found that aircraft data
at one.pressure level (just below cloud base) scattered
along a mixing line, and interpreted this to mean that
air was being sampled from different levels in an at-
mosphere partially mixed by convection. Although here
the air above the CBL is not at present being mixed,
the variation in its thermodynamic structure along a
mixing line suggests that it may have been convectively
mixed in the past. Following Betts (1984), we can con-
clude that the thermodynamic gradients with pressure
just above the inversion follow this mixing line. This
is useful information because it confirms the gradient
suggested by Fig. 5b and 5d.

3) THE θ^* AVERAGE

The average by θ^* was chosen to attempt to resolve
the structure through the inversion. The variations in
the pressure height of the inversion and cloud top as
shown by the lidar data, mean that the p-averaged data
smooths the profile through the inversion. The θ^* av-
erage better preserves the location of data with respect
to.the strong θ gradient, and Fig. 5d shows that the SP
profile continues to follow closely the moist adiabat
through the inversion and changes gradient just below
the inversion top.

The structure of the θ^* average nearer the surface
was a bit surprising (points labeled 968, 946). We be-
lieve this distribution of points represents a combina-
tion of two gradients of the data: the horizontal vari-
ation of θ^* (and correspondingly q^*) probably asso-
ciated with the strong gradient in SST (slope shown as
heavy dashes) and the vertical gradient of θ^* through
the subcloud and lower cloud layers. The insert sche-
matic shows how the addition of these two gradients
might produce the gradient shown. This needs further
study.

4) COMPOSITE MEAN STRUCTURE FROM THE VERTICAL PROFILES

Figure 6 shows a mean thermodynamic profile
through the CBL based on subsections 1–3. We col-
lected the p average data into larger bins with roughly
the same number of points in each (typically 300–500
values) to generate a smoother profile. The composite
profile follows this p-averaged profile from 995 to 915
hPa and then the θ^* average through the inversion.
The p average at 903 hPa (solid circle, labeled T) is the
thermodynamic mean for air above the inversion (900
$< p < 905$ hPa). This point, which is important to our
subsequent budget analysis, is well established since it .
lies on the approximate mixing line shown in the p^*
composite. There is still some uncertainty. in the tran-
sition through the inversion (915–905 hPa), and the
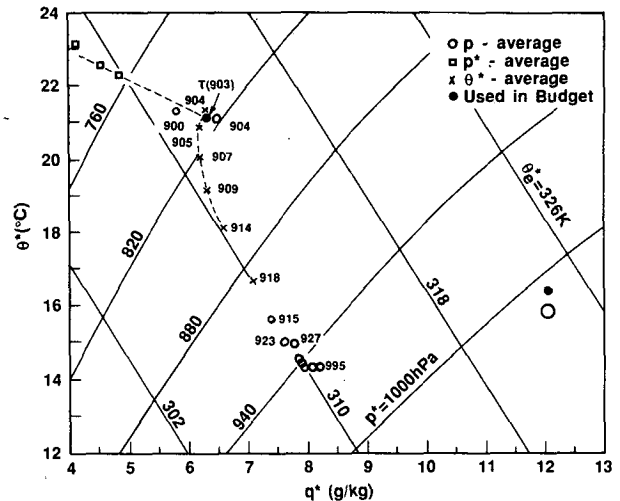gradient above. A dashed line is drawn through the

FIG. 6. Composite mean SP plot using p and θ^* averaging.

inversion and above the inversion following the prob-
able SP structure to demonstrate that there appears to
be a kink there, perhaps associated with the radiative
cooling at cloud top. There is a small inconsistency
between'the two points marked 915 and 918 where we
switch from the p to the θ^* average: this is a measure
of the uncertainty in the structure near the inversion
base, which varies in pressure. The cloud and subcloud
layer structure will be shown in greater detail in Fig. 9
(see later).

Figures 7a, b show a conventional plot against pres-
sure of the average profiles of θ^* [which is close to a
$\theta(p)$ profile but becomes $\theta_l(p)$ in the cloud layer], and
the horizontal wind velocity magnitude $|U|$. The sur-
face pressure and temperature are 1008 hPa and 17°C,
and a corresponding value of θ^* is shown. We note
that there is an air–sea temperature difference of about
2°C, so the layer is being driven by significant surface
heating. The surface fluxes (see §4a) are fairly large
because the low level wind is large; in fact, the lowest
aircraft level at about 100 m above the surface has the '
maximum wind for the CBL. There is a strong shear
through the inversion layer with weak winds above.

5) MEAN VALUES OF dp^*/dp

Betts (1986) suggested that the parameterization of
the CBL in global models could be simplified by using
a mixing line model and a parameter

$$\beta = dp^*/dp \qquad (1)$$

for the mean gradient of saturation level with pressure.
For a well-mixed layer $\beta = 0$, and typical cumulus
layers have $\beta \approx 1.0$. Figures 3 and 4 show that this
stratocumulus-capped CBL is not well-mixed. In Fig.
8, we show an average for the ascent-descent profiles
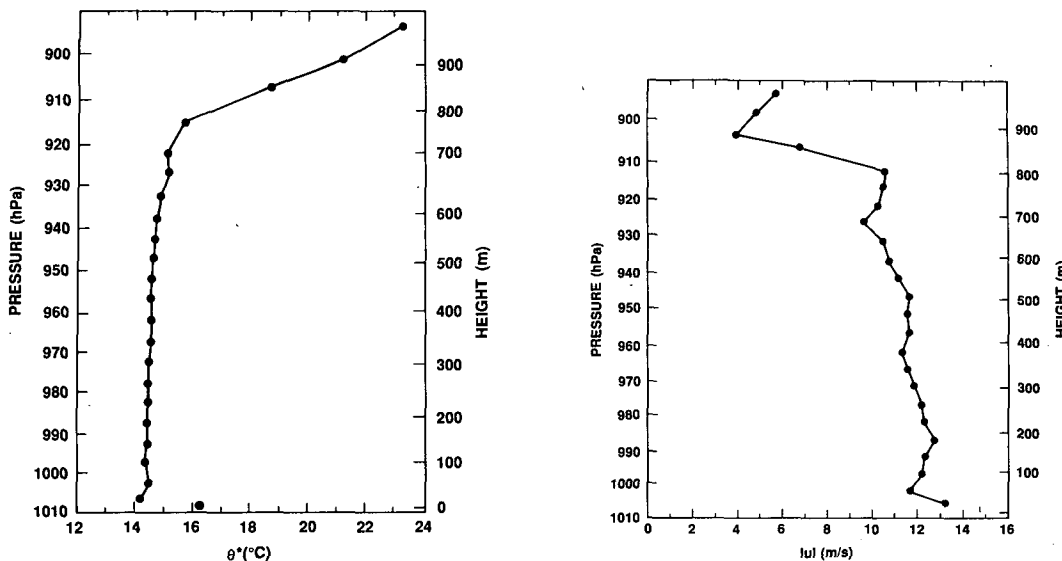on a p^*–p plot (The data was collected into 10 hPa

FIG. 7. (a, b) Profiles of θ^* and $|U|$ as function of pressure.

bins in p before averaging). In the subcloud layer $\beta \approx 0.1$ although some scatter in the data is visible. The gradient dp^*/dp changes in the cloud layer: $\beta \approx 0.4$ near cloud-base and then, in this composite, increases rapidly. Since the cloud layer varied in thickness from 100–400 m, this $p^*(p)$ is somewhat smoothed by the variation of cloud top. Individual profiles in p^* showed considerable variation, but $\beta \approx 0.4$ (with an uncertain error) is a reasonable mean value for this stratocumulus layer. This value is used to construct liquid water profiles for the radiation model (see §4b)

d. Partition into ascending and descending branches

1) INTRODUCTION

A lot of data was collected from a few horizontal legs flown in the cloud layer. Following the stratocumulus circulation model presented in Betts (1983), we

decided to partition the data into ascending and descending subsets, and look at the distribution of SP about the mean for each. Although the partitioning is usually done with the vertical velocity, this data was considered somewhat suspicious near aircraft turns. Because there was a strong shear through the CBL, with light winds aloft and a wind maximum near the surface (Fig. 7b), we used the magnitude of the horizontal wind, U, as a tracer to determine whether air had ascended or descended to a given level. The procedure was as follows: for each data leg, a linear trend line was fitted to the U values; and for data points above (below) this mean trend, the p^* and T^* values were put into the ascent (descent) categories. This is a very simple procedure, but in the cloud layer where the mean shear is strong, it probably gave a satisfactory partition of the data. In the subcloud layer where the shear is weaker, the separation may be less satisfactory. All the data including the ascent–descent legs were partitioned in this way. Mean values and distributions about the mean were generated for T^*, and p^* for the ascending and descending air.

2) MEAN SP PAIRS FOR CLOUD LAYER

Figure 9 shows the SP pairs for ascending and descending air partitioned using the horizontal wind as described above. Three pairs are shown: and for three layers in the cloud layer: $910 < p < 920 < p < 930 < p < 950$ (including only data with positive LWC), and an average for the whole subcloud layer $950 < p < 1000$ hPa (solid circle) The mean profile from Fig. 6 is shown on this expanded scale. The dashed line indicates the slope of the dry virtual adiabat $\theta_v = 15.8°C$ through the subcloud layer mean SP, showing that
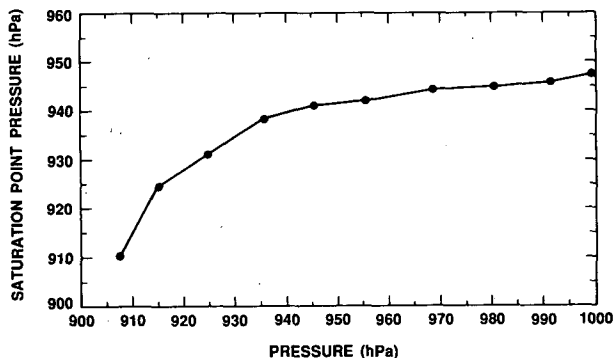

FIG. 8. Plot of p^* versus p averages for all in-cloud and subcloud data.
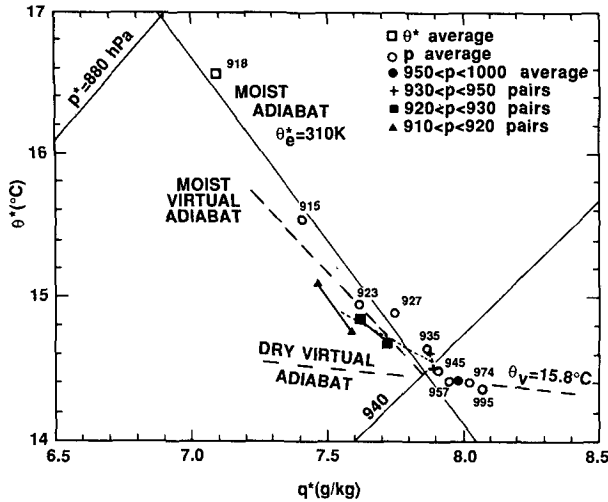
FIG. 9. Mean composite profile with SP pairs in cloud layer.

above the superadiabatic surface layer, the subcloud structure is not far from being neutral to dry processes.

The cloud layer pairs at 915 (i.e., $910 < p < 920$) and 925 hPa are dominated by the horizontal legs, and they have a slight offset in SP from the mean sounding. This reflects simply the selection of the subset of the data, with positive liquid water content. There are differences in slope of the ascent–descent pairs in the cloud layer. For an idealized circulation (Betts, 1983) this slope is related to the circulation stability, and the time dependence of the layer. The pair at 925 hPa which contains most of the horizontal cloud leg data is unstable to the moist virtual adiabat, suggesting that the cloud circulation has positive kinetic energy generation. The highest level data pair at 915 hPa (for which there is less data) is slightly stable to the moist adiabat, but has the same slope as the mean SP profile through the cloud layer. This shift of slope with height towards a more stable gradient is consistent with the analysis of Betts (1983) for an idealized unsteady stratocumulus circulation (see §4). However, there is also a strong gradient in the radiative cooling rate through the cloud layer (see §4b), with radiative heating for $p > 925$ hPa. We believe the more stable structure in the mean SP profile near cloud base (between points at 945 and 935 hPa) and the very stable structure for the ascent/descent pair near cloud base ($930 < p < 950$) reflect this radiative warming near cloud base. The line joining the means of each cloud level SP pair gives a second mean profile (shown dotted) for data within cloud (liquid water positive). It lies between the dry and moist virtual adiabats, again indicating positive kinetic energy generation within the cloud layer. It is more unstable than the composite mean profile which includes all data (not just in-cloud data). In section 4, we shall estimate the entrainment rate, the internal circulation velocity and

the time dependence from these data, using in addition flux estimates from a radiative model, and at the surface using bulk aerodynamic formulae.

3) DISTRIBUTION OF SP ABOUT THE MEAN FOR UP/DOWN PAIRS

We proceeded by separating the data in the cloud layer into pressure level intervals of 10 hPa and computed the $(p^* - \bar{p}^*)$, $(T^* - \bar{T}^*)$ histograms for each of these levels, where $\bar{p}^*$, $\bar{T}^*$ are the average SP pressure and temperature for each flight leg. Some statistics are given in Table 1. While the updraft-downdraft separation of SPs increased as pressure decreased, so did the spread of SPs around the average. The variances in p^*, T^* for the descent branch was consistently higher by 2 to 3 hPa and 0.1 to 0.2°C than the corresponding variances for the ascent branch. This difference indicates more homogeneity for ascending air than for descending air. We can define a signal-to-noise ratio for the separation of SP pairs as

$$\text{SN}_{p^*} = \frac{\Delta p^*}{\bar{\sigma}_{p^*}}, \quad \text{SN}_{T^*} = \frac{\Delta T^*}{\bar{\sigma}_{T^*}} \qquad (2)$$

where Δp^* is the difference between mean SP values for ascending and descending branch, and $\bar{\sigma}_{p^*}$, $\bar{\sigma}_{T^*}$ are the standard deviations, averaged over ascending and descending branches. We found that the signal-to-noise ratio varied from ~ 0.3 near cloud base to 1.11 near the cloud top, with almost equal values for SN_{p^*} and SN_{T^*}. The reduction in quality of separation further down in the layer is probably a result of our conditional sampling analysis using horizontal velocity magnitude which showed less of a gradient in the subcloud layer than in the cloud layer. It might also be that below cloud base the two branches lose their separate identity. Figure 10 shows the p^*-T^* histograms for the pressure in $920 < p < 930$ (for which there was the most data). The ordinate is the number of samples in each 1 hPa, 0.1°C interval. There are more downdraft samples (1610) than updraft (1492) so the difference in the peaks may not be significant. The downdraft distribution has a larger variance because its distribution has broader wings. The overlap of the distributions is not surprising considering the horizontal inhomogeneities in the data.

4) SPECTRAL STRUCTURE OF SP

We performed a spectral analysis on the saturation-point pressure time series to investigate which horizontal length scales contributed mostly to the saturation point variance. Only horizontal legs below the inversion were included in this analysis as large gradients in the inversion would contaminate the spectral computations. Also, the ascent and descent flight legs were excluded because of variable gradient in the vertical of the saturation point pressure as witnessed from the p^*-

TABLE 1. Separation of updraft–downdraft SPs (hPa, °C).

	$\overline{p^*}, \overline{T^*}$	σ_{p^*, T^*}	$\bar{\sigma}_{p^*, T^*}$	$\Delta p^*, T^*$	SN_{p^*, T^*}
		$900 < p < 910$			
p^* updraft	916.54	8.86	11.75	13.01	1.10
p^* downdraft	903.53	13.2			
T^* updraft	8.34	0.49	0.64	0.69	1.07
T^* downdraft	7.66	0.71			
		$910 < p < 920$			
p^* downdraft	928.60	6.95	8.86	8.10	0.91
p^* downdraft	920.50	10.55			
T^* updraft	8.72	0.39	0.48	0.38	0.80'
T^* downdraft	8.35	0.55			
		$920 < p < 930$			
p^* updraft	934.01	5.64	6.9	5.62	0.81
p^* downdraft	928.39	7.97			•
T^* updraft	9.10	0.361	0.39	0.32	0.83
T^* downdraft	8.78	0.42			
		$930 < p < 950$			
p^* updraft	940.45	4.01	4.80	1.96	0.41
p^* downdraft	938.49	5.58			
T^* updraft	9.51	0.25	0.30	0.05	0.17
T^* downdraft	9.45	0.34			

p plot (Fig. 8). Because of the orientation of the clouds in north–south directions only east–west flight legs were included to facilitate a direct comparison with the lidar data. All data were interpolated linearly onto a regular spaced grid of 80 m (1 s data, average aircraft speed 80 m s^{-1}). This was necessary because of the variable ground speed. Next, sections of 128 points (9.6 km) were detrended, cosine tapered at 10% of the data interval to dampen spurious wave modes (Otnes and Enochson, 1978) because of the finite length of the data

sections, and then Fourier transformed. A more sophisticated filtering procedure, such as used in BSH for the cloud-top data, could not be used since the SP time series were so short in comparison with the lidar data sections. Individual spectra usually had multiple peaks. The largest peaks were found between 3 and 5 km with smaller secondary peaks at 1 to 3 km.

Figure 11 shows the spectrum averaged for all the individual spectra, each were normalized by their variance. Eighteen spectra were used to compute the av-
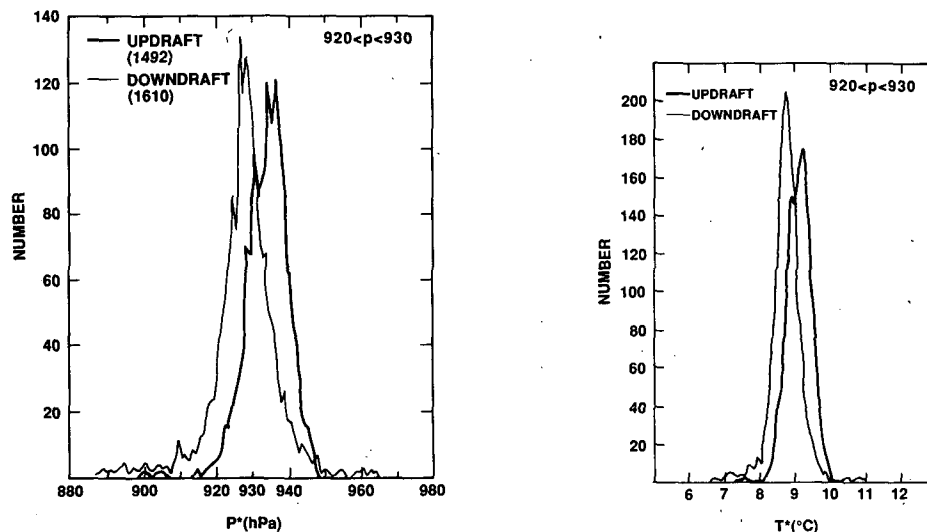
FIG. 10. (a, b) p^*–T^* histograms for updraft sampled between 920 and 930 hPa.
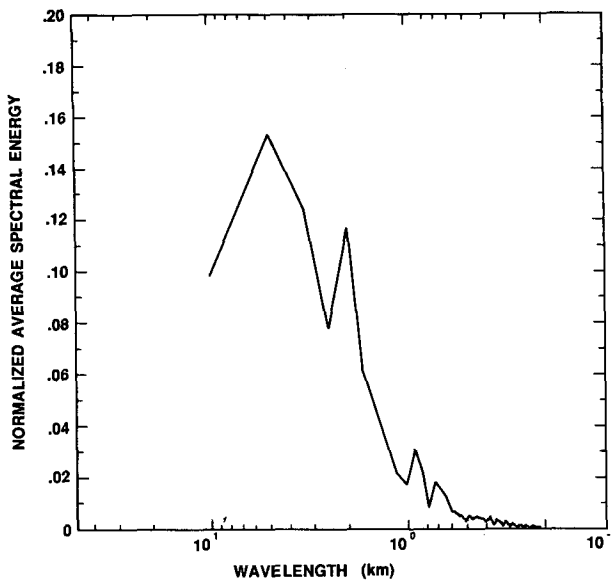
FIG. 11. Average spectrum of time series of p^* for horizontal flight legs (in cloud and below the inversion) in an east–west direction.

erage. The average spectrum contains two significant peaks: a primary peak at 5 km, and a secondary peak at 2 km. Two smaller peaks are visible at scales smaller than 1 km. The spectral peak at 5 km agrees very well with the dominant spectral peaks found for the lidar cloud top data and the *M*ultispectral *C*loud *R*adiometer (MCR) aboard the NASA ER-2 (see BSH). It corresponds to the dominant cloud size found in the experimental area. The rather large peak at 2 km is less easily explained. It is more pronounced than similar peaks found for the lidar data, but not inconsistent with the smaller cloud sizes as evidenced from the MCR reflectance data and available cloud pictures (see BSH). Perhaps, the strength of the signature in the lidar spectra at 2 km does not reflect the strength of the internal cloud circulations at those scales. The accurate agreement of locations of the main spectral peaks in the lidar, MCR, and saturation point data establishes beyond reasonable doubt that the dominant CBL circulation scale in east–west direction for this case study was approximately 5 km, or six times the mean depth of the PBL. Consequently, the mean spacial separation between up- and downdrafts as characterized by the SP pairs and variances presented in the previous section, was about 2.5 km.

4. Budget analysis of layer

We shall present an approximate budget analysis for the layer following Betts (1983), to show that useful information can be extracted from the mean structure about the entrainment, internal circulation and time dependence.

a. Surface flux estimates

We first estimate the surface fluxes from the differences $\Delta\theta$ and Δq between the sea surface and the lowest level aircraft data using a bulk aerodynamic method.

$$F_{Cp\theta} = \rho_0 C_p C_T V_0 \Delta\theta \qquad (3)$$

$$F_{Lq} = \rho_0 L C_T V_0 \Delta q. \qquad (4)$$

Table 2 summarizes the computation.

The surface wind speed V_0 was taken from the level of the lowest aircraft data at 995 hPa. The bulk transfer coefficient $C_T = 1.05 \times 10^{-3}$ was taken from Stage and Businger (1981), and the sea surface temperature was taken as 17°C from satellite SST data (courtesy of NOAA). There is a strong north–south temperature gradient of approximately 1°C/100 km across the experimental region and the low level wind flow is from the north.

The surface sensible and latent heat fluxes of 31 and 156 W m^{-2} are moderate values: the convection is being driven by surface heating as air flows over a warmer ocean.

b. Radiative flux estimates

No radiative flux measurements were available for this flight so a radiative model was used to estimate both long and shortwave contributions to the radiative fluxes using the distribution of cloud top heights available from the lidar (BSH), and the in situ liquid water information, parameterized using a mixing line model (see section 2d).

1) RADIATION MODEL

The radiative heating and cooling rates were calculated using a one-dimensional radiative flux model similar to that used in the UCLA/GLA GCM (Harshvardhan et al., 1987). The model includes longwave and solar components, and can be used for clear sky or partially cloudy conditions. The vertical resolution

TABLE 2. Estimation of surface fluxes.

Level (hPa)	V (m s^{-1})	T (°C)	θ (°C)	q (g kg^{-1})	$\Delta\theta$ (°C)	Δq g kg^{-1}	$F_{cp\theta}$ W m^{-2}	F_{Lq} W m^{-2}
1008		17.00	16.34	12.05				
995	12.1	13.95	14.36	8.07	1.98	3.98	31.00	156

is arbitrary: we computed fluxes and heating/cooling rates every 5 hPa within the subcloud and stratocumulus layers. The longwave model accounts for absorption and emission by water vapor, carbon dioxide and ozone, and treats clouds as multilayer absorbers which are nearly black, but with single-layer emissivities based on cloud liquid water. The shortwave model includes absorption by water vapor, absorption by ozone above any cloud layer, nonconservative multiple scattering by cloud droplets, and direct and diffuse reflection by the earth's surface. More details on the radiation model can be found in Betts and Ridgway (1988).

The radiative model requires that a few parameters and the important vertical atmospheric thermodynamic profiles be specified. Surface temperature is needed and surface albedos for scattering of direct and diffuse solar radiation are specified, along with the solar zenith angle. A climatological carbon dioxide concentration and a reference ozone mixing ratio profile are also used within the model. The key vertical profiles are temperature, humidity, and liquid water content within clouds, and separate temperature and humidity profiles for clear regions. A clear-air sounding above the CBL was constructed from the mean thermodynamic profiles (Figs. 6, 7a), the aircraft ascent and descent soundings into the experiment area and the nearby Oakland sounding at 00Z 28 September 1983. The temperature, moisture and liquid water profiles within clouds were reconstructed for a series of cloud top heights, using a mixing line model.

2) MIXING LINE MODEL FOR STRATOCUMULUS THERMODYNAMIC PROFILES

The lidar information gave us a distribution of cloud top heights over the area. For the radiation computation, we ignored the variation of cloud base. The in situ data gave us mean thermodynamic profiles, av-
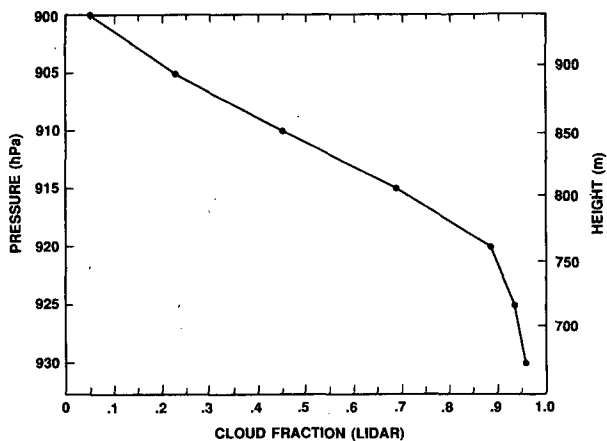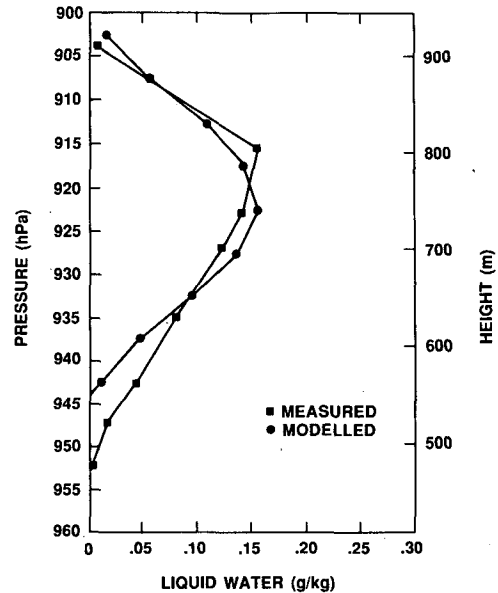
FIG. 13. Comparison of observed and model liquid water, computed using a mixing line model.

eraged over all the data collected, and bulk estimates of their gradients with pressure in the cloud and subcloud layers, parameterized in terms of $\beta = dp^*/dp$. We reconstructed profiles of temperature, water vapor, and liquid water, for a range of cloud top heights from 930 to 900 hPa, using a mixing line model (Betts, 1985a), computed radiative fluxes for each, and then weighted the radiative fluxes by the distribution of cloud tops. This cloud top distribution with pressure is shown in Fig. 12. It includes only cloud data in the area of the in situ aircraft pattern. In this region there was a 95% cloud cover. A single mixing line was used to represent the mean thermodynamic gradients between the base of the subcloud layer and the highest sampled in-cloud data at 915 hPa. Consistent with Fig. 8, a value of $\beta = 0.08$ was used for the subcloud layer. This gives a cloud-base of 942 hPa, our best estimate of a mean cloudbase. In the cloud layer, (model) cloud water increases with height up to one level (5 hPa) below each cloud top, where it falls linearly to zero at cloud top. The temperature at the cloud-top boundary is computed and used in the radiation computation. The cloud-layer value of β was adjusted to reproduce the mean observed in situ liquid water content. Good agreement was found for $\beta = 0.4$, which is consistent with the mean cloud-layer profile of $p^*(p)$ near cloud base discussed in section 3b(5). Figure 13 shows the comparison. The observed profile of the liquid water content is simply that from the pressure average of all the data. The model profile is computed using a mixing line model with $\beta = 0.4$ for a range of cloud tops from 930 to 900 hPa, weighted with the distribution of tops observed by lidar. The profile shapes appear similar,

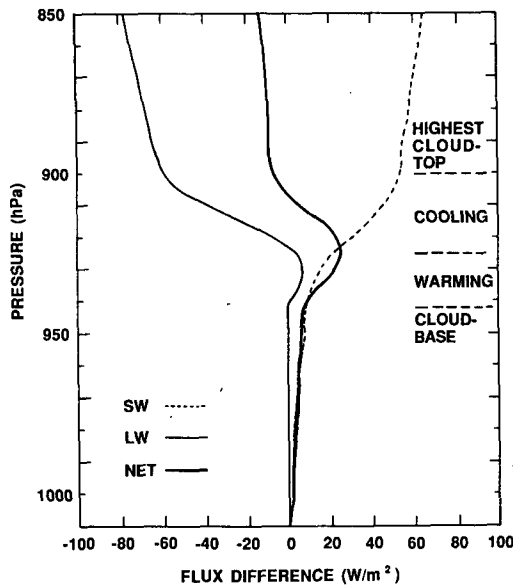FIG. 12. Fractional cloudiness shown as a function of cloud-top pressure.

FIG. 14. Shortwave, longwave and net radiation flux difference from surface through the boundary layer as a function of pressure.

although the two peaks are displaced by about 5–7 hPa. The observed LWC profile however, is based on data which has an inhomogeneous distribution with pressure. The data point at 922.5 hPa represents three times as much data as that at 915 hPa, so the apparent displacement of the peak may not be significant.

3) RADIATION FLUX PROFILES

Figure 14 shows shortwave, longwave, and the net radiative fluxes through and above the boundary layer, differenced from the surface values (positive downwards). There is a flux divergence, and therefore, strong cooling in the upper part of the cloud layer from 925–900 hPa, and strong warming below between 945 (cloud-base) and 925 hPa. Qualitatively, the mean SP profile shown in Figs. 6 and 9 is consistent with this net radiative flux. The destabilization of the in-cloud data [see §3d(2)] with respect to mixing with inversion top air is consistent with the strong radiative cooling from 925–900 hPa, as air sinks slowly through the inversion. The smaller stable kink in the SP profile from

945–935 hPa (see Fig. 9) is, we believe, associated with the net radiative heating in the lower part of the cloud layer. This kink is small because the internal circulation velocity is fast near cloud base. There is slight warming of the subcloud layer. Table 3 summarizes the flux divergences (ΔN) for different layers which will be used to estimate the entrainment rate (next section). The flight is shortly after local noon when the solar absorption is at a maximum, so the boundary layer as a whole has only a small radiative cooling (8 W m^{-2}). However, the cloud layer has a strong heating-cooling couplet of 25–35 W m^{-2} [comparable to the surface sensible heat flux (Table 2)], which destabilizes and generates kinetic energy within the cloud layer, and drives additional entrainment.

c. Budget equations for layer

If we integrate through the stratocumulus layer to generate a mixed layer representation, we obtain the mean budget equation (see appendix B).

$$\frac{\Delta p}{g}\frac{D\bar{M}}{Dt} = \rho_0 C_T V_0 (O - M_0)$$

$$+ \rho_e W_e(T - \bar{M}) + \Delta N/C_p \quad (5)$$

where $\bar{M}$ is the mean SP of the boundary layer (from 1008 to an average stratocumulus top of 913 hPa), M_0 is the mean SP at the lower aircraft data level of 995 hPa (see Table 2), D/Dt is the horizontal Lagrangian time derivative and O and T are the SPs of the ocean surface and air above the inversion. We shall take these as (17°C, 1008 hPa) and (4.16°C, 813 hPa) respectively. The ΔN is the radiative flux divergence across the whole layer and it is small and known. W_e is the entrainment rate at cloud top. We know $\rho_0 C_T V_0$ and M_0 [see (4a)], so that the time rate of change of the layer can be found if we can estimate W_e [see (4f)].

We simultaneously consider the budget for a thin layer below cloud top of thickness δp with mean SP, $\bar{M}^1$. The budget equation for this layer is (see appendix B).

$$\frac{\delta p}{g}\frac{D\bar{M}^1}{Dt} = F_1 + (\omega_e/g)(T - M_1') + \Delta N_1/C_p \quad (6)$$

where F_1 is the convective flux at the base of the layer

TABLE 3. Entrainment rates.

Pressure (hPa)	ΔN (W m^{-2})	ω_e/g ($\times 10^{-2}$ kg m^{-2} s)	W_e (cm s^{-1})	ω^*/g ($\times 10^{-2}$ kg m^{-2} s^{-1})	W^* (cm s^{-1})
900–1008	−8.0 ΔN				
900–915	−23.2 ΔN_1	0.92	−0.81	9.4	8.2
900–925	−33.0 ΔN_2	1.19	−1.04	17.5	15.3
	Mean values	1.06	−0.93	13.5	11.8

(a distance δp below the cloud top) and the entrainment velocity has been replaced by a mass flux defined by $\omega_e/g = \rho_e W_e$ [kg m^{-2} s^{-1}]. The M'_1 is close to the mean SP at the base of this layer and is defined precisely in appendix B; ΔN_1 is the net radiative flux difference across this layer. We can parameterize F_1 in terms of a convective mass circulation (Betts, 1983):

$$F_1 = (\omega^*/g)(A - D)_1 \qquad (7)$$

where ω^*/g is a convective mass flux (in kg m^{-2} s^{-1}) and $(A - D)_1$ the SP difference between ascending or descending branches of the circulation. Then

$$gF_1 = \omega^*(A - D)_1$$

$$= -\omega_e(T - M'_1) - g\Delta N_1/C_p + \delta pD\bar{M}^1/Dt. \qquad (8)$$

Let us define a T'_1 by (Betts, 1983)

$$g\Delta N_1/C_p = \omega_e(T'_1 - T). \qquad (9)$$

Then

$$\omega^*(A - D)_1 = -\omega_e(T'_1 - M'_1) + \delta p\frac{D\bar{M}^1}{Dt}. \qquad (10)$$

We shall assume that although the layer is evolving in time,

$$D\bar{M}^1/Dt = D\bar{M}/Dt. \qquad (11)$$

This will be justified retrospectively when we find the circulation time scale is an order of magnitude less than the adjustment time scale for the layer as a whole (see section g).

Equation (5) can be reexpressed as (Betts, 1983)

$$\Delta pD\bar{M}/Dt = (\omega_0 + \omega_e)(E - \bar{M}) \qquad (12)$$

where $\omega_0 = \rho_0 gC_D V_0$, representing an approach to an equilibrium state E which satisfies

$$0 = \omega_0(O'' - E) + \omega_e(T'' - E) \qquad (13)$$

where T'' is defined as a shift produced by the radiative flux divergence [analogous to (9)] by

$$g\Delta N/C_p = \omega_e(T'' - T) \qquad (14a)$$

and O'' is given by

$$O'' = O + (M - \bar{M}_0). \qquad (14b)$$

This correction arises because the layer is not well mixed and the surface flux is given by $\omega_0(O - M_0)/g$, not by $\omega_0(O - M)/g$.

Graphically (see section 4f), E lies on the mixing line between O'' and T'' [which can be found knowing T, ΔN, and ω_e using (14a)]. Clearly, we can find E if we can find ω_e.

Substituting (11) and (12) in (10) gives with rearrangement

$$\omega^*/\omega_e(A - D)_1 = (M'_1 - T_1)$$

$$+ (\delta p(\omega_0 + \omega_e)/\Delta p\omega_e)(E - \bar{M}) = (M'_1 - L) \qquad (15)$$

where

$$L_1 = T_1 + (\delta p(\omega_0 + \omega_e)/\Delta p\omega_e)(\bar{M} - E). \qquad (16)$$

We can solve (15), which has two components, for ω^* and ω_e. Our procedure will be to find the point L in (16) (which depends only on known variables T, O, M'_1, ω_0, ΔN, ΔN_1) and ω_e, by varying ω_e until $(M'_1 - L_1)$ is parallel to $(A - D)_1$, which is given by the ascent/descent SP pairs. We have aircraft data at two different levels near cloud top, so we can get two independent estimates of ω_e. Equation (15) then gives a corresponding value of ω^* for each level.

Equations (15) and (16) show that as the thickness of a budget layer near the CBL top increases, $\delta p/\Delta p$ increases, and $(L - T)$ increases in the direction of $(\bar{M} - E)$, the lag of the layer from equilibrium. We see [Eqs. (15), (16) and Fig. 9] that this corresponds to a rotation of $(A - D)$ as we go down through the CBL from cloud top. This rotation of $(A - D)$ is related to the time air takes to circulate in a time-dependent layer (see Fig. 7 in Betts, 1983).

d. Entrainment rate

We solved (15) and (16) for two thin layers near cloud top using the aircraft data at 915 and 925 hPa partitioned into ascending and descending branches to give $(A - D)$ (section 3d). The mean cloud top from the lidar data was 913 hPa, so the 915 hPa layer is close to cloud top. There is strong radiative cooling above 925 hPa which corresponds to a level of maximum downward net flux (Fig. 14). (For $p < 925$ hPa, the cloud is cooling radiatively, and for $p > 925$ hPa, it is warming; 925 hPa is also approximately the level of maximum computed mean liquid water content in the radiation model (Fig. 13).

Table 3 shows the net radiative flux differences for the whole layer (ΔN) and for 900 to 915 hPa and 925 hPa (ΔN_1, ΔN_2, respectively). From these we derive two independent estimates of the entrainment mass flux (ω_e/g) of 0.9 and 1.2 10^{-2} kg m^{-2} s^{-1} corresponding to entrainment velocities (W_e) of 0.8 and 1.0 cm s^{-1}. The agreement is satisfactory, considering the computation is based on a radiation model using independent lidar data, and on aircraft data from different levels. Indeed, it is perhaps remarkable that such consistent estimates are obtained. The 915 hPa level is close to cloud top so the difference $(L - T)$ in (16) is small, but there is six times as much aircraft data at the 925 hPa level. Nicholls and Leighton (1986) and Nicholls and Turton (1986) in a study of stratocumulus over UK coastal waters found entrainment rates from data typically of order 0.5 cm s^{-1}, about half our value. Most of their stratocumulus cases, however, were uncoupled from the surface, whereas here, the surface-sensible heat flux is comparable to the radiative flux divergence across the top of the cloud layer. Also, large

shear was present at the cloud top, so our value of W_e ≈ 0.9 cm s^{-1} is not unrealistic.

There are, however, several possible sources of error in this estimate. The assumptions in the radiation model (Betts and Ridgway, 1988), which relate the shortwave and longwave fluxes to the liquid water, have not been fully tested against data. This is one of the objectives of the First ISSCP (International Satellite Cloud Climatology Project) Regional Experiment. There is uncertainty in the computation (which could introduce an error in $W_e \approx 20\%$), associated with defining cloud top, and the choice of a layer for the radiative flux divergence ΔN, because cloud top is not uniform. The average cloud top is 913 hPa from the lidar data with a variance on small-scales (<10 km) of order 4 hPa and a gradient with cloud top increasing from east to west by more than 20 hPa (I). We have composited all the aircraft and lidar data to construct one mean budget for the volume. The radiation computation shows the perturbation in the radiative fluxes is confined below 900 hPa (Fig. 14). In the radiation computation, there were no cloud tops higher than 900 hPa, and 74% of the cloud tops were for $p \geqslant 910$ mb. So we chose to estimate ΔN from 900 hPa (Table 3). We also chose the average cloud top as 913 hPa (from the lidar data) to estimate δp and Δp. This is not entirely satisfactory since the in-cloud aircraft data at 915 hPa (used for A − D) is almost certainly biased towards cloud tops at a lower pressure, with probably the reverse bias for the aircraft data at 925 hPa. The effect of these unknown biases is to increase our estimate of W_e from the 915 hPa data and reduce W_e from the 925 hPa data, and it may account for the difference in the estimates.

The other major source of inaccuracy lies in the slopes of the updraft–downdraft vectors, (A − D), obtained from partitioning and averaging the aircraft data. These slopes constrain the convective fluxes near cloud top and the entrainment rate, but their accuracy is hard to assess. As well as small residual errors in the dewpoint and liquid water data (section 2), there is in addition, much larger variability associated with horizontal gradients and inhomogeneities in the cloud field. The distributions of (T^*, p^*) about the mean at, say, 925 hPa, show (Fig. 10) that the separation of updraft and downdraft means is comparable to the variance of each. In meteorology, this is often true of composite studies. However, no satisfactory general method exists for assessing the statistical significance of composite profiles that are widely used to extract a consistent vertical structure from data which have large horizontal variability.

Nevertheless, the structure shown in Fig. 9 for the mean profile and the gradients of the in-cloud SP pairs seems physically reasonable, and the resulting budgets give two largely independent but consistent estimates for the entrainment rate, which cannot be measured directly.

Our budget also completely neglected any fallout of liquid water, but this may be reasonable because the cloud layer on average was less than 300 m thick.

e. Convective mass circulation

The solution of (15) also gives values for the convective mass circulation (ω^*/g) at 915 and 925 hPa (Table 3). These are an order of magnitude larger than ω_e, corresponding to circulation velocities $W^* \approx 10$ cm s^{-1}. There is an indication that ω^* decreases from 925 to 915 hPa, as cloud top is approached, which is to be expected. Penc and Albrecht (1987) found similar values (5–10 cm s^{-1}) in stratocumulus off the west coast of the USA.

f. Budget diagram

Figure 15 shows the layer budget diagram; the saturation points are listed in Table 4. The points O, $\bar{M}$ and T for the ocean surface (solid circles), layer mean SP, and the air above the inversion are known, along with ω_0, the surface flux velocity scale. Here O″ is defined by (14b) to allow for the SP gradient in the subcloud layer. O′ is an SP corresponding to a cooler sea surface temperature (16°C).

Figure 15 was constructed by solving (15) and (16) as discussed earlier. Two solutions are shown: suffix 1, and 2. Solutions T''_1, E_1, T_1 and L_1 were determined using the 915 hPa aircraft data and the corresponding points, with suffix 2, using the 925 hPa level data. The two solutions are independent associated with different values of ΔN_1, ΔN_2, and slightly different estimates of ω_e (Table 3). The points T_1, T_2 and T''_1, T''_2 are defined
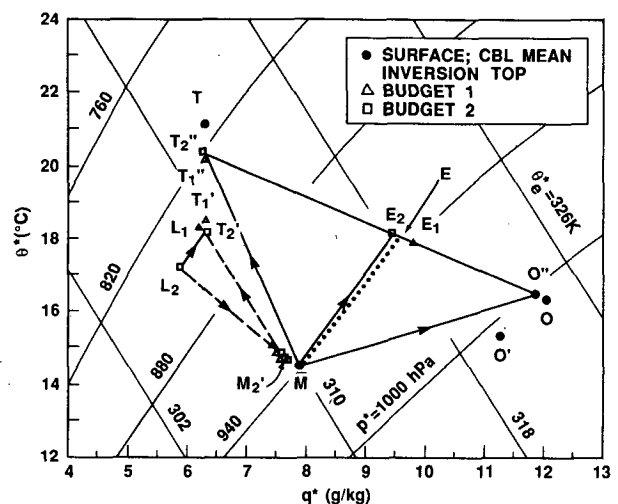

FIG. 15. Saturation-point budget diagram showing time rate of change of layer mean, M, towards equilibrium state, E, determined by two cloud top budgets using aircraft data at 915 and 925 hPa (suffices 1 and 2, respectively). The O, T are SPs of the ocean surface (17°C, 1008 hPa) and the air above the cloud top inversion, respectively (see text for other symbols).

TABLE 4. Saturation points for budget diagram (Fig. 15).

Point	N	p (hPa)	T^* (°C)	p^* (hPa)	θ^* (°C)	q^* (g kg^{-1})	θ_e^* (K)
O		1008.0	17.00	1008.00	16.34	12.05	323.9
O'		1008.0	16.00	1008.00	15.34	12.20	320.6
O"		1008.0	16.71	1002.60	16.49	11.88	323.6
M		960.5	9.50	940.46	14.51	7.89	310.1
T		902.8	4.16	813.00	21.08	6.32	312.8
A₁	265	914.8	8.72	928.60	14.76	7.59	309.5
D₁	243	914.8	8.35	920.50	15.10	7.46	309.5
M'₁		914.8	8.54	924.72	14.92	7.52	309.5
T"₁		913.0	4.33	823.44	20.19	6.32	311.8
E₁		960.5	12.75	939.72	17.87	9.81	319.2
L₁		914.8	4.45	843.18	18.32	6.22	309.6
T'₁		913.0	4.69	843.96	18.50	6.32	310.0
A₂	1492	924.2	9.10	934.01	14.67	7.74	309.9
D₂	1610	924.2	8.78	928.39	14.84	7.62	309.7
M'₂		924.2	8.92	930.73	14.77	7.67	309.8
T"₂		913.0	4.29	821.05	20.39	6.32	312.1
E₂		960.5	12.02	927.86	18.19	9.47	318.6
L₂		924.2	3.74	846.51	17.25	5.89	307.5
T'₂		913.0	4.74	847.11	18.24	6.32	309.8

by (9) and (14a) and can be thought of an entrained inversion-top air modified by a radiative flux divergence. The solid lines show the mean vector budget represented by Eqs. (12) and (13), for the 925 hPa aircraft data (suffix 2). The dotted line, the average of E_1 and E_2, gives a mean estimate for the time dependence of the layer. We have found the mean time dependence of an unsteady layer from the in-situ data and the radiative flux computation. The dashed lines correspond to the cloud-top layer budget represented by (15) for the 925 hPa data. The convective flux vector ($\mathbf{M}_2 - \mathbf{L}_2$) is parallel to ($\mathbf{A}_2 - \mathbf{D}_2$), which are the open squares on either side of $\mathbf{M}_2$. The vector ($\mathbf{T}'_2 - \mathbf{M}_2$) represents the sum of the entrainment and radiative cooling for this layer. The resultant is ($\mathbf{T}'_2 - \mathbf{L}_2$), which is parallel to ($\mathbf{E}_2 - \mathbf{M}$), the time dependence vector for the layer mean.

g. Time scales for stratocumulus layer

Betts (1983) showed that there were two important timescales for a stratocumulus layer: an external adjustment time scale for the layer τ_E given by (17) and an internal circulation time scale τ_I.

Equation (11) can be rearranged to express the time rate of change of the layer as

$$D\bar{\mathbf{M}}/Dt = (\mathbf{E} - \bar{\mathbf{M}})/\tau_E \qquad (16)$$

where

$$\tau_E = \Delta p/(\omega_0 + \omega_e). \qquad (17)$$

Here τ_E is the adjustment time of the layer mean: a measure of the lag of the layer from equilibrium with the underlying sea surface, the net radiative flux divergence and the entrainment of dry, warm air from above. The τ_I is defined as

$$\tau_I = \Delta p/2\omega^* \qquad (18)$$

which is a measure of the time air takes to make half a mean circuit (e.g., top to bottom) of the layer. Taking from Table 3 mean values of $\omega_e/g = 1.1 \ 10^{-2}$ kg m^{-2} s^{-1}, and $\omega^*/g = 14 \ 10^{-2}$ kg m^{-2} s^{-1} gives corresponding time scales of

$$\tau_E \approx 10 \text{ h}, \quad \tau_I \approx 1 \text{ h}.$$

We see that $\tau_I \ll \tau_E$, so that for the mean time evolution, ($\mathbf{E} - \bar{\mathbf{M}}$), we may regard the layer as approximating a well-mixed layer. In terms of Fig. 15, we find that the spread of SP within the layer (although measurable by aircraft) is much less than other typical vectors such as ($\bar{\mathbf{M}} - \mathbf{T}''$), ($\mathbf{O}'' - \bar{\mathbf{M}}$), associated with the fluxes at the boundaries.

h. Time dependence and sea surface temperature (SST) gradient

The lag of the layer from equilibrium is the vector ($\bar{\mathbf{M}} - \mathbf{E}$) on Fig. 15. The air in this boundary layer has been advected over a warmer ocean in a northerly flow with a strong north–south oceanic temperature gradient. We have plotted on Fig. 15 a SST, $\mathbf{O}'$, of 16°C as well as 17°C (our estimate for the local SST), to show the direction of the SST gradient (at constant pressure) on a θ^*-q^* diagram. We see that ($\mathbf{E} - \bar{\mathbf{M}}$) is roughly parallel to ($\mathbf{O} - \mathbf{O}'$) and corresponds to about a 3°C change of sea surface temperature. The layer adjustment time of 10 hours, together with a mean layer advection speed of order 11 m s^{-1} gives an advection distance for this adjustment of order 400 km. The SST 400 km to the north is indeed about 14° or 3°C colder. We conclude that the budget diagram is

consistent with advection over warmer water with a lag time of about 10 hours, related to $\Delta p/(\omega_0 + \omega_e)$. Although we have no observational evidence, the boundary layer, while strongly time-dependent because of the large surface gradient, could be in a quasi-steady state with respect to a moving equilibrium point E. Little change was seen locally in the cloud deck during the 2½ hours of observational time.

5. Conclusions

The present analysis shows what we believe to be the first detailed account of the saturation point structure of a stratocumulus cloud layer. Although east Pacific stratocumulus clouds are frequently thought of as stationary, this study provides an example of an unsteady layer with substantial upward fluxes of heat and moisture at the surface and strong horizontal advection. To arrive at a mean vertical structure, we combined a p and θ^* average of saturation point parameters. The saturation point structure of the layer consists of three branches, one extending from near cloud base down to the surface SP, one through the cloud layer and the other from near cloud top upward into the inversion. Tendency towards stationarity can be seen as tendency of the layer to smooth out the "kinks" between the lines. However, this tendency is counteracted by cloud top cooling, cloud-base warming, and advection over a warmer sea surface. The thermodynamic structure of the layer above the inversion is also characterized by a mixing line suggesting it was convectively mixed in the past.

The internal circulation was resolved by separating the SPs into updrafts and downdrafts depending on the magnitude of their horizontal velocities. This was possible because of the strong horizontal shear through the cloud layer. The results indicate that the mixing lines formed by updraft-downdraft pairs of SPs (averaged over p interval bins) are correlated with the radiative heating and cooling profile. Analysis of the variance of p^*, T^* values around this average indicates that updraft air is consistently more homogeneous than downdraft air, which is modified by entrainment and radiative cooling. An SP separation signal-to-noise ratio was defined to indicate the quality of separation between up- and downdraft SP pairs. It appeared that for this cloud layer, the SP separation signal-to-noise ratio decreased towards the subcloud layer. A spectral analysis was performed on the in-cloud saturation pressure data. The primary contribution to the p^* variance was found at horizontal scales of 5 km, with a secondary peak at 2 km. The 5 km peak corresponds very well to the 4.5 km peak in the lidar cloud-top height variance spectra reported by BSH. It indicates that the observed cloud-top height variability is a representation of the internal boundary layer structure. The 5 km peak suggests that the mean separation between ascending and descending branches of the cloud circulation is 2.5 km.

We have drawn a budget diagram for the time dependent boundary layer based on the ideas of Betts (1983), and derived the cloud-top entrainment rate from the partitioning of the in situ aircraft data into ascending and descending air, the lidar top data and a radiation model. We believe this is the first analysis of this kind, which shows that the entrainment rate and time evolution can be estimated without detailed in-cloud flux data. Our mean value of the entrainment rate of $W_e = 0.9$ cm s^{-1} seems reasonable for a layer which has strong radiative, shear as well as surface forcing. The internal circulation mass flux is an order of magnitude larger than the entrainment rate, consistent with the internal structure, and with other studies (Penc and Albrecht, 1987).

The external adjustment time (τ_E) associated with the lag of the layer from equilibrium with the ocean surface is of order 10 hours. This corresponds to an advection distance of order 400 km. The SST gradient over this distance agrees fairly well with the vector lag $(\mathbf{E} - \bar{\mathbf{M}})$ of the layer from equilibrium. This suggests that the layer may be internally in a quasi-steady state, even though not in equilibrium with the ocean. The internal circulation time scale τ_I is of order 1 h, an order of magnitude less than τ_E, which suggests that a quasi-steady internal structure may exist as the layer evolves in time.

APPENDIX A

Response Time Correction for Dewpoint

As discussed in section 2a, our procedure to correct the dewpoint was to replace $T_{dew}(t + 2)$ by $T_{dew}(t)$. We found that the 2-second delay time was, in almost all cases, sufficient to line up the peaks in temperature and valleys in dewpoint for inversion air, and to match closely dewpoint and temperature for cloudy air. More significantly, it provided a remarkable improvement of the SP structure for inversion level air. We show Figs. A1a, b. Both figures represent θ^*-q^* diagrams corresponding to the data shown earlier in Fig. 1. The only difference between Fig. A1a, and A1b is that for A1a, the original data has been used, while for A1b,
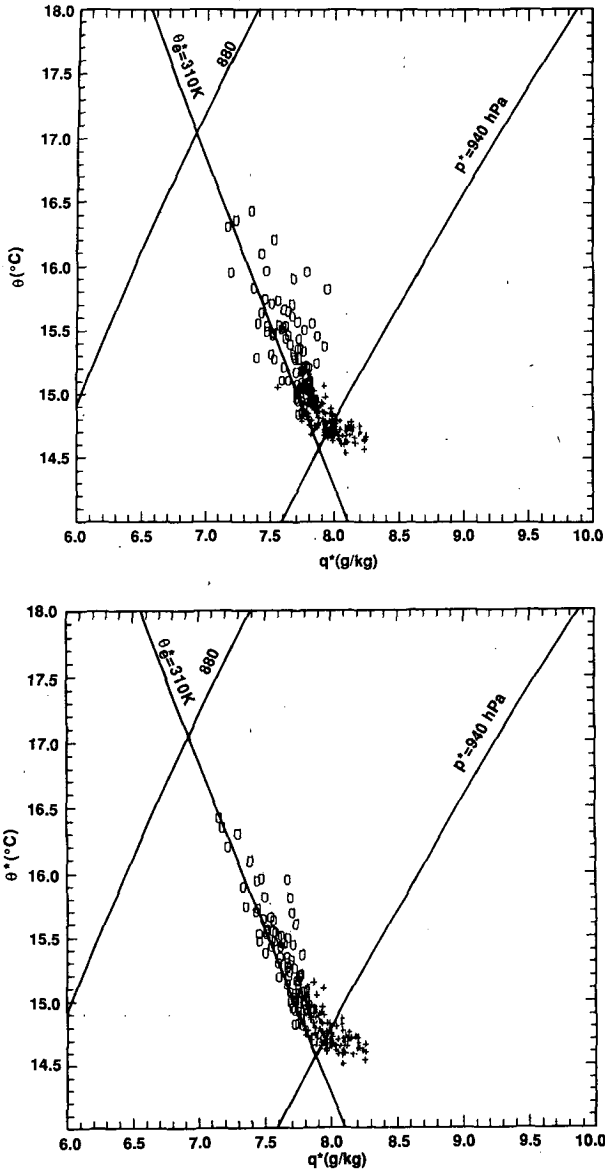
FIG. A1. (a) Skew-T diagrams of the same flight leg, (from Fig. 1) but for (b) the dewpoint time-shifted by 2 seconds.

the filtered and time-shifted dewpoints were used. Points with liquid water content below 0.02 g m^{-3} are marked with zeros; those with higher liquid water content, by pluses. It is seen that in this second plot, the scatter in points representing inversion air with no or very small liquid water content is dramatically reduced. The scatter can be explained as follows: when the aircraft enters a cloud from the inversion, the temperature suddenly falls, while the dewpoint increases accordingly. However, since the dewpoint lags behind, there will be a number of SPs with the characteristics of cold dry air; hence, some will fall to the left of the bulk part of the scatterplot. When the aircraft exits the cloud, the situation is reversed: temperature rises suddenly,

while the dewpoint lags behind in falling. Consequently, some SPs will seem to originate from warm, moist parcels and fall to the right of the scatterplot. As expected, the in-cloud data with higher liquid water content in the bottom of the diagram is hardly affected by this procedure. Although a significant portion of the scatter in SP is reduced by this procedure, it does not completely remedy the lag problems of the instrument. Nevertheless, the internal structure and circulation characteristics are well resolved by this data.

APPENDIX B

Derivation of Budget Equations: (5) and (6)

Betts presented the thermodynamic budget equations for a well mixed stratocumulus layer using SP variables. Betts, (1984, 1985b) and Betts and Simpson (1987) extended these ideas to show the thermodynamic budgets as two-dimensional vector diagrams. We here extend the analysis to a partially mixed time-dependent stratocumulus layer.

We integrate down from a pressure p_T just above the inversion capping the stratocumulus layer to an arbitrary level p_1 to give a mean budget equation for the layer: p_1 to p_T.

$$\frac{D}{Dt}\int_{p_T}^{p_1} \mathbf{M} dp = \mathbf{M}_1 \frac{Dp_1}{Dt} - \mathbf{T}\frac{Dp_T}{Dt} + \int_{p_T}^{p_1} (D\mathbf{M}/Dt)dp$$

(B1)

Here D/Dt denotes the horizontal Lagrangian time derivative, $\mathbf{M}$ is the mean profile of SP within the CBL, and $\mathbf{M}_1$, $\mathbf{T}$ are the SPs at p_1, p_T, respectively.

Substituting the budget equation,

$$D\mathbf{M}/Dt = -\omega\partial\mathbf{M}/\delta p + g\partial\mathbf{F}/\partial p + (g/C_p)\partial\mathbf{N}/\partial p \quad (B2)$$

where $\mathbf{F}$ is the convective SP flux associated with the stratocumulus circulation and $\mathbf{N}$ the net radiative flux (both positive upward) and defining a mean value

$$\int_{p_T}^{p_1} \mathbf{M} dp = \bar{\mathbf{M}}^1(p_1 - p_T) \quad (B3)$$

gives, with some manipulation (and replacing D/Dt by the overdot)

$$(p_1 - p_T)\dot{\bar{\mathbf{M}}}^1 = (\omega_T - \dot{p}_T)(\mathbf{T} - \mathbf{M}_1) + (\omega_T - \omega_1)(\mathbf{M}_1$$
$$- \tilde{\mathbf{M}}^1) - (\dot{p}_T - \dot{p}_1)(\mathbf{M}_1 - \bar{\mathbf{M}}^1) + g\mathbf{F}_1 + g\Delta\mathbf{N}_1/C_p$$

(B4)

where $\Delta\mathbf{N}_1$ is the net radiative flux difference from p_T, where $F_T = 0$, and $\tilde{\mathbf{M}}^1$ is a vertical average weighted by the horizontal mass divergence. We shall assume horizontal divergence independent of height so that $\tilde{\mathbf{M}}^1 = \bar{\mathbf{M}}^1$, and define the entrainment rate as

$$\omega_e = \omega_T - \dot{p}_T. \quad (B5)$$

If we integrate down to the surface, and let $\omega_1 = \dot{p}_1$

= 0, the budget equation for the whole layer becomes (dropping the superscript)

$$(p_0 - p_T)\dot{\mathbf{M}} = g\mathbf{F}_0 + \omega_e(\mathbf{T} - \bar{\mathbf{M}}) + g\Delta\mathbf{N}/C_p. \quad \text{(B6)}$$

Substituting $\Delta p = p_0 - p_T$ for the CBL depth, and

$$\mathbf{F}_0 = \rho_0 C_T V_0(\mathbf{O} - \mathbf{M}_0) \quad \text{(B7)}$$

for the surface flux gives Eq. (5). The only approximation we have made is to set $\mathbf{M} = \bar{\mathbf{M}}$: the neglect of any vertical structure in the horizontal mass divergence, for which we have no data. Since the variation of $\mathbf{M}$ is small, this approximation is also probably small.

The second budget equation involves a thin layer of thickness $\delta p = p_1 - p_T$ near cloud top. We shall assume $(\omega - \dot{p})$ varies linearly with pressure so that

$$(\omega_T - \dot{p}_T) - (\omega_1 - \dot{p}_1) = (\delta p/\Delta p)\omega_e. \quad \text{(B8)}$$

This is equivalent to considering a layer p_1 to p_T which is a fixed fraction of the CBL depth, as well as constant horizontal divergence, so that again $\tilde{\mathbf{M}}^1 = \bar{\mathbf{M}}^1$. Substituting (B8) and (B5) in (A4) gives Eq. (6)

$$\delta p\dot{\mathbf{M}}^1 = g\mathbf{F}_1 + \omega_e(\mathbf{T} - \mathbf{M}'_1) + g\Delta\mathbf{N}_1/C_p \quad \text{(6)}$$

where we have defined

$$\mathbf{M}'_1 = \mathbf{M}_1(1 - \delta p/\Delta p) + \bar{\mathbf{M}}_1(\delta p/\Delta p).$$

Since $(\delta p/\Delta p)$ is small, $\mathbf{M}'_1$ is close to $\mathbf{M}_1$ the value at the base of the layer, and the assumption inherent in (B8) is of little importance.

REFERENCES

Albrecht, B. A., A. K. Betts, W. Schubert and S. K. Cox, 1979: A model for the thermodynamic structure of the trade-wind boundary layer: Part I. Theoretical formulation and sensitivity tests. *J. Atmos. Sci.*, **35**, 73–89.

Betts, A. K., 1982a: Saturation point analysis of moist convective overturning. *J. Atmos. Sci.*, **39**, 1484–1505.

——, 1982b: Cloud thermodynamics models in saturation point coordinates. *J. Atmos. Sci.*, **39**, 2182–2191.

——, 1983: Thermodynamics of mixed stratocumulus layers: Saturation point budgets. *J. Atmos. Sci.*, **60**, 2655–2670.

——, 1984: Boundary layer thermodynamics of a high plains severe storm. *Mar. Wea. Rev.*, **112**, 2199–2211.

——, 1985a: Mixing line analysis of clouds and cloudy boundary layers. *J. Atmos. Sci.*, **42**, 2751–2763.

——, 1985b: Vector representation of trade cumulus thermodynamic fluxes. *Mon. Wea. Rev.*, **113**, 2173–2175.

——, 1986: A new convective adjustment scheme. Part I: Observational and theoretical basis. *Quart. J. Roy. Meteor. Soc.*, **112**, 677–691.

——, and B. A. Albrecht, 1987: Conserved parameter analysis of the convective boundary layer thermodynamic structure over the tropical ocean. *J. Atmos. Sci.*, **44**, 83–99.

——, and J. Simpson, 1987: Thermodynamic budget diagrams for the hurricane subcloud layer. *J. Atmos. Sci.*, **44**, 842–849.

——, and W. Ridgway, 1988: Coupling of the radiative, convective, and surface fluxes over the equatorial Pacific. *J. Atmos. Sci.*, **45**, 522–536.

Boers, R., J. D. Spinhirne and W. D. Hart, 1988: Lidar observations of the fine-scale variability of marine stratocumulus clouds. *J. Climate Appl. Meteor.* (to be published).

Brost, R. A., D. H. Lenschow and B. L. Wyngaard, 1982: Marine stratocumulus layers part I: Mean conditions. *J. Atmos. Sci.*, **39**, 800–917.

——, J. C. Wyngaard and D. H. Lenschow, 1982: Marine stratocumulus layers Part II. Turbulence Budgets. *J. Atmos. Sci.*, **39**, 818–836.

Cooper, W. A., 1978: Cloud physics investigations by the University of Wyoming in HIPLEX, 1977. University of Wyoming Rep. 119. [Available from the Dept. of Atmos. Science, University of Wyoming, Laramie, WY, 82071.]

Deardorff, J. W., 1980: Cloud top entrainment instability. *J. Atmos. Sci.*, **37**, 131–147.

Duchon, C. E., and J. S. Goers, 1976: Variance spectrum analysis of aircraft dewpoint measurement system noise. *J. Appl. Meteor.*, **15**, 77–93.

Friehe, C. A., R. L. Grossman and Y. Pann, 1986: Calibration of an airborne Lyman-Alpha hygrometer and measurement of water vapor flux using a thermoelectric hygrometer. *J. Atmos. Oceanic Technol.*, **3**, 299–306.

Greenhut, G. K., and S. J. S. Khalsa, 1982: Updraft and downdraft events in the atmospheric boundary layer over the equatorial Pacific Ocean. *J. Atmos. Sci.*, **39**, 1803–1818.

Hanson, H. P., 1984: On mixed layer modeling of the stratocumulus topped marine boundary layer. *J. Atmos. Sci.*, **61**, 1226–1236.

Harshvardhan, R. Davies, D. A. Randall and T. G. Corsetti, 1987: A fast radiation parameterization for atmospheric circulation models. *J. Geophys. Res.*, **92**, 1009–1016.

Lilly, D. K., 1968: Models of cloud topped mixed layers under a strong inversion. *Quart. J. Roy. Meteor. Soc.*, **96**, 292–308.

Nicholls, S., and J. Leighton, 1986: An observational study of the structure of stratiform cloud sheets. Part I: Structure. *Quart. S. Roy. Meteor. Soc.*, **112**, 631–550.

——, and J. D. Turton, 1986: An observational study of the structure of stratiform cloud sheets. Part II: Entrainment. *Quart. J. Roy. Meteor. Soc.*, **112**, 641–680.

Otnes, A. K., and L. Enochson, 1978: *Applied Time Series Analysis, Vol. 1.* Wiley and Sons, 449 pp.

Paluch, I. R., 1979: The entrainment mechanism in Colorado cumulus. *J. Atmos. Sci.*, **36**, 2467–2478.

Penc, R. S., and B. A. Albrecht, 1987: Parametric representation of heat and moisture fluxes in cloud-topped mixed layers. *Bound. Layer Meteor.*, **38**, 225–248.

Randall, D. A., 1980: Entrainment into a stratocumulus layer with distributed radiative cooling. *J. Atmos. Sci.*, **37**, 148–159.

Schubert, W. H., J. S. Wakefield, E. F. Steiner and S. U. Cox, 1979: Marine stratocumulus convection: Part I. *J. Atmos. Sci.*, **36**, 1286–1307.

Slingo, A., S. Nicholls and J. Schmetz, 1982: Aircraft observations of marine stratocumulus during JASIN. *Quart. J. Roy. Meteor. Soc.*, **108**, 833–856.

Stage, S. A., and J. A. Businger, 1981: A model for the entrainment into a cloud topped boundary layer. Part I. Model description and application to a cold air outbreak. *J. Atmos. Sci.*, **38**, 2213–2229.

Suarez, M. J., A. Arakawa and D. A. Randall, 1983: The parameterization of the planetary boundary layer in the UCLA general circulation model. Formulation and results. *Mon. Wea. Rev.*, **111**, 2224–2243.